ACCEPTED MANUSCRIPT

Journal of Applied Physics

AIP Publishing

This is the author's peer reviewed, accepted manuscript. However, the online version of record will be different from this version once it has been copyedited and typeset.

PLEASE CITE THIS ARTICLE AS DOI: 10.1063/5.0076959

Dynamic Routing through Saturable Absorption in Graphene Photonic Resonators: Impact of Carrier Diffusion and Finite Relaxation Time

Georgios Nousios,[1, a)] Thomas Christopoulos,[1] Odysseas Tsilipakos,[2] and Emmanouil E. Kriezis[1]
[1)] *School of Electrical and Computer Engineering, Aristotle University of Thessaloniki (AUTH), Thessaloniki GR-54124, Greece*
[2)] *Institute of Electronic Structure and Laser, Foundation for Research and Technology-Hellas (FORTH-IESL), GR-71110 Heraklion, Crete, Greece*

(Dated: December 31, 2021)

We assess the continuous wave and dynamic routing performance of a compact silicon-on-insulator disk resonator overlaid with a graphene monolayer at telecommunication wavelengths. Switching action is enabled by saturable absorption in graphene, controlled by a pump wave of only few milliwatts. Graphene saturable absorption is modeled through a carrier rate equation that incorporates both the finite relaxation time and diffusion of photo-generated carriers, providing a realistic account of carrier dynamics. The overall nonlinear response of the resonator is evaluated with a rigorous mathematical framework based on perturbation theory and temporal coupled-mode theory. We thoroughly investigate the effects of carrier diffusion and finite relaxation time, both separately and in conjunction. We also take into account nonlinear refraction via a Kerr effect term and quantify its impact on the overall response. In order to suppress the Kerr effect, we replace silicon with silicon-rich nitride, allowing for the individual contributions of the resonator core and graphene (of opposite sign) to exactly compensate each other. Our results contribute to the understanding of carrier dynamics and their impact on the performance of practical graphene-based switching components.

I. INTRODUCTION

Graphene is the most prominent and well-studied two-dimensional (2D) material; it has attracted great scientific interest and has found a wide variety of applications in electronics and photonics[1] being compatible with the commercial CMOS and silicon-on-insulator (SOI) platforms. Especially in photonics, graphene exhibits a broadband optical response from the THz regime to the near infrared (NIR) with its linear surface conductivity being dynamically tunable through an externally applied electric field,[2] rendering graphene a highly promising material for electro-optic modulators.[3–6] Furthermore, graphene exhibits a strong nonlinear response, with its third-order susceptibility reported to be orders of magnitude higher than that of conventional bulk materials such as semiconductors, chalcogenide glasses, and nonlinear polymers.[7–10]

One of most notable nonlinear effects in graphene is saturable absorption (SA), i.e., the nonlinear quenching of losses with increasing optical power due to Pauli blocking. Graphene SA is characterized by ultra-fast response and low power requirements;[11,12] it is thus attractive for a number of photonic applications including passive mode-locked lasers (MLL),[13–15] all-optical switching elements,[16–18] and modulators.[19] The study of graphene nonlinearities, including saturable absorption, is under intense investigation with the physical and mathematical description slowly maturing. A number of both theoretical and experimental works[20–23] have recently appeared, aiming to find an accurate and comprehensive model for graphene SA, as well as to investigate its interplay with other physical effects in the overall nonlinear response. Apart from SA, there has also been significant scientific progress in comprehending the nonlinear refraction effect of graphene, referred to as the saturable photo-excited carrier refraction (SPCR) effect.[24,25]

Motivated by the aforementioned developments, in this work we model graphene SA by a phenomenological carrier rate equation that incorporates the finite relaxation time and diffusion of photo-generated carriers, thus allowing for a realistic description of carrier dynamics. Saturable absorption in graphene is exploited to lend routing functionality in a practical three-dimensional (3D) SOI disk resonator. The resonator is side-coupled with two bus waveguides and a counter-propagating two-wave excitation (pump-probe) scheme is used to enable routing operation, with the exit port of the probe wave (through or drop port) controlled by the power level of the control wave. The overall nonlinear response is evaluated with a computationally-efficient, rigorous mathematical framework comprising perturbation theory and temporal coupled-mode theory (CMT), fed by linear full-wave simulations.[18,26] The effects of SA finite relaxation time and carrier diffusion are meticulously examined, both separately and in combination, and their impact on dynamic routing performance is assessed. Moreover, nonlinear refraction is taken into account by means of a Kerr term. A practical avenue to suppress the Kerr effect is proposed by substituting silicon with silicon-rich nitride (SRN), which exhibits higher third-order susceptibility, allowing for the respective contributions of SRN (resonator core) and graphene (of opposite sign) to compensate each other.

The rest of the paper is organized as follows: In Sec. II the graphene SA model is described and subsequently in-

---

[a)] Electronic mail: gnnousios@ece.auth.gr

AIP Publishing

corporated in the broader nonlinear mathematical framework. In Sec. III, the proposed framework is applied in a practical graphene-enhanced SOI disk resonant configuration and the nonlinear response is evaluated both in continuous wave (CW) and dynamic conditions. Finally, in Sec. IV offers concluding remarks.

II. THEORETICAL FRAMEWORK

A. Graphene Saturable Absorption with Carrier Diffusion and Finite Relaxation Time

The linear surface conductivity of graphene, σ_1, is determined by both intraband and interband transitions: $\sigma_1 = \sigma_{\text{intra}} + \sigma_{\text{inter}}$. Due to Pauli blocking, the interband transitions are only allowed when graphene is biased below the half-photon energy $|E_{\text{F}}| < \hbar\omega/2$, where E_{F} is the Fermi energy. Moreover, when $|E_{\text{F}}| < \hbar\omega/2$ the interband component dominates over the intraband and graphene is at the high-loss regime. On the other hand, when $|E_{\text{F}}| > \hbar\omega/2$, the interband transitions are prohibited corresponding to the low-loss regime.[27,28] Under strong optical illumination both interband and intraband conductivities exhibit saturation, albeit for different levels of light intensity each. In the NIR (telecommunication wavelengths), interband conductivity saturates for relatively low light intensities $\sim$ MW/cm^2, while intraband conductivity saturates for much larger values $\sim$ GW/cm^2. The latter power regime is beyond any practical interest, while it is further expected that for such high intensities multi-photon processes like two-photon absorption (TPA) would become significant, hindering the practical observation of intraband conductivity saturation.[12] Therefore, in this work we assume that σ_{inter} is the only saturable component of graphene conductivity and subsequently graphene has to be biased below the half-photon energy ($|E_{\text{F}}| < \hbar\omega/2$) for the SA effect to manifest.

Since graphene SA is microscopically attributed to band filling as a direct consequence of the Pauli exclusion principle, a natural way to describe it is via the surface carrier density. In addition, this approach enables the investigation of carrier diffusion and finite relaxation time effects, thus resulting in more precise modeling of the SA phenomenon. In this work we utilize the phenomenological SA model introduced in[21,29]

$$\sigma_{\text{inter}}(N_{\text{c}}) = \sigma_0 \left(1 - \frac{N_{\text{c}}}{2N_{\text{sat}}}\right), \tag{1}$$

where $N_{\text{c}}(x,z)$ is the surface carrier density of graphene, $\sigma_0 \equiv \sigma_{\text{inter}}^{(0)}$ is the unsaturated (low-power) interband conductivity and N_{sat} is a phenomenological carrier saturation density which corresponds to the value of the carrier density where the interband conductivity is halved, $\sigma_{\text{inter}}(N_{\text{sat}}) = \sigma_0/2$.

The aforementioned SA model applies solely to the real part of σ_{inter}. However, it has been suggested theoretically and verified experimentally that the photogeneration of carriers results in the appearance of nonlinear refraction as well. This has been termed SPCR effect[24] and is expected to impact the overall nonlinear response of graphene as it was shown to overshadow the typical third-order ($\chi^{(3)}$) perturbative effects. Furthermore, both SA and SPCR effects occur for the same light intensity regime and hence their interplay should be considered to get an accurate description of graphene nonlinearity. Alternatively, graphene hot electron models (GHEMs) have also been suggested in the literature,[20,23,25] capable of extracting the nonlinear response of graphene through thermodynamic analysis rather than utilizing phenomenological models like Eq. (1), leading to a more accurate and comprehensive description. Such models are still under development, with the suggested frameworks leading in some cases to different results.

In this work, we choose to model the nonlinear refraction effect of graphene as a third-order nonlinear process (Kerr effect) described by a σ_3 conductivity; σ_3 is considered to be power-independent and thus independent from the photo-generated carrier density N_{c}. Although, such a perturbative approach is not as rigorous, especially for high light irradiation where the perturbation assumption is in question, it enables to distinguish and study separately the effects of (i) nonlinear refraction and (ii) carrier diffusion and finite relaxation time. The third-order graphene surface conductivity σ_3 is generally complex, with the imaginary part describing the Kerr effect (self-phase modulation) and the real part the effect of TPA (nonlinear loss). When graphene is biased below the half-photon energy, the dominant absorption mechanism is the first-order interband conductivity, σ_{inter}. Therefore, for $|E_{\text{F}}| < \hbar\omega/2$ two-photon absorption is not practically observed and consequently σ_3 can be considered as purely imaginary.[7,8]

The surface carrier density of graphene is assumed to fulfill the following spatio-temporal carrier rate equation[29]

$$\frac{\mathrm{d}N_{\text{c}}}{\mathrm{d}t} = \frac{\frac{1}{2}\mathrm{Re}\{\sigma_{\text{inter}}(N_{\text{c}})\}\left|\mathbf{E}_{||}\right|^2}{\hbar\omega} - \frac{N_{\text{c}}}{\tau_{\text{c}}} + D\nabla^2 N_{\text{c}}, \tag{2}$$

where $\mathbf{E}_{||}$ is the tangential to graphene electric field, while the spatial dependence of the carrier density $N_{\text{c}} \equiv N_{\text{c}}(x,z)$ is fully-retained. The first term in the right-hand side of Eq. (2) is the source term, derived directly from Ohm's law, while it is also assumed that every photon excites a single electron in the conduction band. We note that the carrier rate equation assumes that carries are generated instantaneously, whereas carrier relaxation occurs in finite time, as modeled by the second term in the right-hand side of Eq. (2). τ_{c} is the phenomenological relaxation time of SA; it encompasses the relaxation times of various physical processes,[30] including the ultrafast intraband carrier-carrier scattering process with typical values in the range 70-200 fs, alongside the much slower intraband carrier-phonon scattering and carrier

ACCEPTED MANUSCRIPT
Journal of Applied Physics
This is the author's peer reviewed, accepted manuscript. However, the online version of record will be different from this version once it has been copyedited and typeset.
PLEASE CITE THIS ARTICLE AS DOI: 10.1063/5.0076959
AIP Publishing

recombination processes with typical values in the range 0.4-1.7 ps.[15,31–33] The relaxation time τ_c has been reported to vary from the fs regime (150 fs in Ref. 21) to the ps-regime (1.67 ps in Ref. 34), as it largely depends on the quality of graphene. Finally, the third term in Eq. (2) describes the in-plane carrier diffusion along the graphene monolayer. Carrier diffusion is expected to have strong impact on the overall nonlinear response when the tangential to graphene electric field is non-uniform, as is the case with strongly-confining integrated photonic elements, e.g., compact waveguides[29] and resonators. On the contrary, diffusion has no tangible effect when graphene is exposed to uniform electric field intensities e.g., continuous graphene layers on a uniform substrate under plane-wave incidence.[34]

Saturable absorption is usually characterized by the saturation intensity I_{sat}, which corresponds to the light intensity under CW operation for which the saturable component of graphene conductivity is halved, $\sigma_{\text{inter}}(I_{\text{sat}}) = \sigma_0/2$. Associating this intensity level with the carrier density N_{sat}, we can write[29]

$$I_{\text{sat}} = \frac{2\hbar\omega N_{\text{sat}}}{\sigma_0 Z_0 \tau_c}, \tag{3}$$

where $Z_0 \approx 377\ \Omega$ is the impedance of free space. In this work, we assume that the SA relaxation time τ_c alongside with the carrier saturation density N_{sat} are intrinsic (microscopic) properties of graphene and independent from each other; the saturation intensity is a macroscopic parameter of graphene, which can be calculated as a function of τ_c and N_{sat} according to Eq. (3). This results in an inversely proportional relation between I_{sat} and τ_c, which has also been derived rigorously in the literature.[12]

B. Rigorous Perturbation and Coupled-Mode Theory Nonlinear Framework

The overall nonlinear response of a graphene-enhanced resonator structure can be evaluated using a rigorous framework combining perturbation theory and temporal CMT. This provides a highly accurate and computational efficient way to study nonlinear resonant elements avoiding the heavy burden of full-wave nonlinear simulations. In the NIR graphene does not contribute to waveguiding, in contrast with the far infrared (FIR) where graphene supports surface plasmon polaritons (SPPs). Thus, its entire presence can be considered as a perturbation affecting only the most-sensitive characteristics of the resonator, resonant frequency and quality factor, without having any substantial effect on the electromagnetic field distribution. Subsequently, the presence of graphene results in a complex frequency shift which can be calculated according to[18]

$$\Delta\tilde{\omega}_{(k)} = \frac{j \displaystyle\iint_S \sigma_1(N_c)\left|\mathbf{E}_{||,(k)}\right|^2 \mathrm{d}S}{\displaystyle\iiint_V \varepsilon_0 \frac{\partial\{\omega\varepsilon_r\}}{\partial\omega}\left|\mathbf{E}_{(k)}\right|^2 \mathrm{d}V + \iiint_V \mu_0\left|\mathbf{H}_{(k)}\right|^2 \mathrm{d}V}, \tag{4}$$

where $\sigma_1 = \sigma_{\text{intra,Re}} + j\sigma_{\text{intra,Im}} + \sigma_{\text{inter}}(N_c)$. In this work, a two-wave excitation scheme is considered, and thus $k = \{c, p\}$ stands for the strong-control (c) and the weak-probe (p) wave, respectively. Note that the surface integral in the numerator of Eq. (4) is calculated on graphene. The volume integral in the denominator is proportional to the total stored energy, taking dispersion of bulk materials into account. Graphene is also a dispersive material, but its dispersion in the NIR is mild and can be omitted;[35] in this case no energy term is associated with the surface current that builds up on graphene,[36] which in any case is considered as a first-order perturbation of the system. The real part of σ_1 results in changes to the quality factor (and, consequently, to cavity photon lifetime), whereas the imaginary part of σ_1 results in a resonant frequency shift. Separating the contributions of real and imaginary parts in Eq. (4), we obtain three different terms $\Delta\omega_{\text{intra},(k)}$, $\tau_{\text{intra},(k)}$ and $\tau_{\text{inter},(k)}(N_c)$. The first two terms describe the contribution of σ_{intra} and they are power-independent; they can be evaluated once (provided that the mode field distribution are first calculated through linear full-wave simulations) and incorporated directly into CMT. On the other hand, the term $\tau_{\text{inter},(k)}(N_c)$ describes the contribution of σ_{inter} and it is power dependent as $N_c(x,z) = N_c\left(\mathbf{E}_{||}(x,z)\right)$. Its incorporation in CMT is possible only by disentangling the spatial and temporal dependencies of the electromagnetic field intensities, while the same disentanglement has to be applied to the spatio-temporal carrier rate equation (2) (see Supplement, Sec. S1).

The Kerr effect can also be incorporated in the CMT framework using first-order perturbation theory. As a multi-wave scheme is considered in this work, the Kerr effect results in two frequency-shift terms for each mode: the first being due to self-phase (SPM) and the second due to cross-phase (XPM) modulation. Besides graphene, the underlying bulk materials of the resonator may also exhibit Kerr nonlinearities and their contributions have to be taken into account. Therefore, the overall frequency shift induced by the Kerr effect is expressed as

$$\begin{aligned}\Delta\omega_{\text{Kerr},(k)} =& \Delta\omega_{\text{SPM},(k)} + \Delta\omega_{\text{XPM},(k\ell)} \\ =& -\left(\gamma^{\text{bulk}}_{\text{SPM},(k)} + \gamma^{\text{gr}}_{\text{SPM},(k)}\right)\left|a_{(k)}\right|^2 \\ & - 2\left(\gamma^{\text{bulk}}_{\text{XPM},(k\ell)} + \gamma^{\text{gr}}_{\text{XPM},(k\ell)}\right)\left|a_{(\ell)}\right|^2,\end{aligned} \tag{5}$$

where $\gamma^{\text{bulk}}_{\text{SPM}}$, $\gamma^{\text{bulk}}_{\text{XPM}}$ are the nonlinear parameters of the bulk materials for SPM and XPM, respectively, whereas $\gamma^{\text{gr}}_{\text{SPM}}$, $\gamma^{\text{gr}}_{\text{XPM}}$ are the respective nonlinear parameters for

Journal of Applied Physics ACCEPTED MANUSCRIPT

This is the author's peer reviewed, accepted manuscript. However, the online version of record will be different from this version once it has been copyedited and typeset.
PLEASE CITE THIS ARTICLE AS DOI: 10.1063/5.0076959

graphene (see Supplement, Sec. S1). Graphene is considered to be a defocusing material in the NIR, thus $\mathrm{Im}\{\sigma_3\} < 0$ and subsequently $\gamma^{\mathrm{gr}} < 0$. Moreover, $a_{(k)}$ is the amplitude of the k mode in the cavity which in CMT is defined to represent the total stored energy of the mode according to: $\left|a_{(k)}\right|^2 \equiv W_{(k)}$.

We can now write the CMT equations for an arbitrary travelling-wave resonator side-coupled to two waveguides as

$$\begin{aligned}\frac{\mathrm{d}a_{(k)}}{\mathrm{d}t} = {} & j\left[-\left(\omega_{(k)} - \omega_{0,(k)}\right) + \Delta\omega_{\mathrm{intra},(k)} + \Delta\omega_{\mathrm{Kerr},(k)}\right] a_{(k)} - \\ & \left(\frac{1}{\tau_{\mathrm{intra},(k)}} + \frac{1}{\tau_{\mathrm{inter},(k)}(N_{\mathrm{c}})} + \frac{1}{\tau_{\mathrm{rad},(k)}} + \frac{1}{\tau_{\mathrm{e},(k)}^{\mathrm{low}}} + \frac{1}{\tau_{\mathrm{e},(k)}^{\mathrm{upp}}}\right) a_{(k)} + j\sqrt{\frac{2}{\tau_{\mathrm{e},(k)}^{\mathrm{low}}}}\, s_{\mathrm{in},(k)},\end{aligned} \tag{6a}$$

$$s_{\mathrm{thr},(k)} = s_{\mathrm{in},(k)} + j\sqrt{\frac{2}{\tau_{\mathrm{e},(k)}^{\mathrm{low}}}}\, a_{(k)}, \tag{6b}$$

$$s_{\mathrm{dr},(k)} = j\sqrt{\frac{2}{\tau_{\mathrm{e},(k)}^{\mathrm{upp}}}}\, a_{(k)}, \tag{6c}$$

where the slowly-varying envelope approximation has been employed and the $\exp\{+j\omega t\}$ time-harmonic convention has been adopted. $\omega_{0,(k)}$ is the resonant frequency, $\omega_{(k)}$ is the operating frequency, and $\tau_{\mathrm{rad},(k)}$ is the radiative cavity photon-lifetime of the k mode, while $\tau_{\mathrm{e},(k)}^{\mathrm{upp/low}}$ is the external cavity photon-lifetime due to the coupling of the k mode to the two waveguides (upper and lower). These parameters are evaluated through linear full-wave simulations solving the eigenvalue problem of the resonator. The input and output waves, $s_{\mathrm{in},(k)}$ and $s_{\mathrm{thr/dr},(k)}$, respectively, are normalized in order to express the input and output powers of the k mode according to: $\left|s_{\mathrm{in},(k)}\right|^2 \equiv P_{\mathrm{in},(k)}$ and $\left|s_{\mathrm{thr/dr},(k)}\right|^2 \equiv P_{\mathrm{thr/dr},(k)}$.

The cavity-amplitude CMT equation, Eq. (6a), is solved concurrently with the spatio-temporal carrier rate equation, Eq. (2), in order to extract the overall nonlinear response of the resonator. This means that a spatial carrier diffusion problem on graphene is solved simultaneously with the two nonlinear ordinary differential equations of CMT.

III. SATURABLE-ABSORPTION-INDUCED ROUTING WITH A GRAPHENE-ENHANCED DISK RESONATOR

Having presented the theoretical framework, we are now in a position to apply it in a practical 3D resonant configuration and study the impact of SA finite relaxation time and carrier diffusion in the structure, both separately and in conjunction.

A. Physical Structure

Given the focus of this work, we choose to study a resonant structure similar to the one presented in Ref. 18. The system is depicted in Fig. 1, consisting of a SOI-based disk resonator overlaid with a monoatomic graphene layer and being side-coupled to two bus waveguides in an add-drop configuration. The tangential to graphene electric field distribution (norm $|\mathbf{E}_{||}|$) is also included for the control wave that excites the $m = 14$ azimuthal order mode of the disk (radial order $q = 1$). This surface graph indicates the respective distribution of carriers that will be generated [cf. Eq. (2)]. The radius of the resonator is $R = 1.503\ \mu$m, in order for the radiative losses to be sufficiently small, while its height ascribes a standard value of 340 nm. The two bus waveguides have the same height as the resonator, while their width is 200 nm. The entire structure is encapsulated in $\mathrm{SiO_2}$ so that a planar surface is available for graphene to reside on, avoiding buckling and mechanical issues. We note here that the waveguides cross-section dimensions were chosen to provide acceptably strong waveguiding while the radius of the resonator was chosen to ensure satisfactory light confinement at acceptable radiation losses.[18] As already mentioned, a two-wave (pump-probe) counter-propagating excitation scheme is studied where the output port of the weak probe wave is dictated by the power level of the strong control wave.

We opt for the following power-dependent routing operation scenario: In the absence of the control wave, the probe wave is transmitted to the through port, whereas for an appropriate control input power the losses of graphene are quenched, the critical coupling condition is met, and the probe wave is steered to the drop port. The input power of the weak probe wave is considered to be constant (CW) and equal to $P_{\mathrm{in},(p)} = 1\ \mu$W; this power

Journal of Applied Physics

ACCEPTED MANUSCRIPT

This is the author's peer reviewed, accepted manuscript. However, the online version of record will be different from this version once it has been copyedited and typeset.

PLEASE CITE THIS ARTICLE AS DOI: 10.1063/5.0076959

AIP Publishing

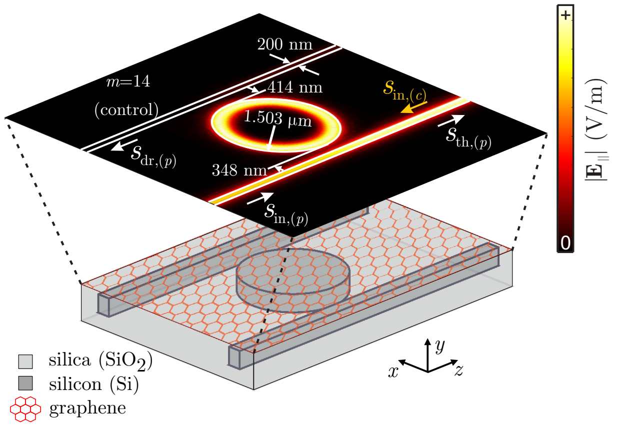

Figure 1. Schematic of the resonator structure under study: A graphene monolayer is overlaid on top of an integrated silicon-on-insulator disk add-drop filter. Norm of the tangential to graphene electric field, $|\mathbf{E}_{||}|$, for the control wave that excites the $m = 14$ azimuthal order mode; it indicates the spatial distribution of carriers that will be generated. The geometric parameters and input/output wave ports are included.

level is too small to induce any nonlinearity. Both control and probe input waves are coupled to the resonator through the lower waveguide [cf. Eqs. (6)]. For this operating scenario, the coupling gaps between the resonator and waveguides are determined to be[18] $g_{\mathrm{low}} = 348$ nm and $g_{\mathrm{upp}} = 414$ nm (for the lower and upper waveguide, respectively), so that the critical coupling condition is met at the high power regime. It is also possible to design for meeting the critical coupling condition in the low (linear) power regime; in this case, the probe wave is switched to the through port in the high-power state. However, with this approach it is not possible to obtain high extinction ratio for the drop port resulting to poor routing performance (see Supplement, Sec. S2).

The first-order conductivity of graphene is determined by the well-known Kubo formula,[27,28] assuming a Fermi energy $E_{\mathrm{F}} \approx 0$ eV and a temperature of $T = 300$ K. Thus, at 1550 nm we find $\sigma_{\mathrm{intra}} = 0.3 - j3.4$ µS and $\sigma_0 \equiv \sigma_{\mathrm{inter}}^{(0)} = 60.9$ µS. The third-order conductivity (which is purely imaginary, see Sec. II) is $\sigma_3 = -j1.2 \times 10^{-20}$ S(m/V)^2.[9,10] We also note that σ_3 has a dependency on graphene Fermi energy,[20] hence its value is carefully chosen to be in accordance with the Fermi energy we consider in this work ($E_{\mathrm{F}} \sim 0$). For the remaining materials, silicon has a linear refractive index of $n_0^{\mathrm{Si}} = 3.48$ and a nonlinear one of $n_2^{\mathrm{Si}} = 2.5 \times 10^{-18}$ m^2/W. For the operating power in this work (few mW), the TPA effect as well as the TPA-originating free-carrier effects (FCE) in silicon[37] have a negligible effect.[18] Linear and nonlinear refractive indices of silica are $n_0^{\mathrm{SiO_2}} = 1.45$ and $n_2^{\mathrm{SiO_2}} = 2.6 \times 10^{-20}$ m^2/W, respectively. Both silicon and silica are considered lossless, while their dispersion is mild and is therefore omitted.

Initially, full-wave linear simulations are conducted using COMSOL Multiphysics® to extract the resonant wavelengths, the quality factors and the field profiles of the two modes in order to specify the corresponding nonlinear Kerr parameters (coefficients in CMT); they are summarized in Table I. Their expressions can be found in the Supplement, Sec. S1. The mode exploited by the probe wave is the $m = 13$ azimuthal-order mode, whereas for the control mode $m = 14$ (radial order $q = 1$ in both cases).

Table I. Resonant wavelengths, quality factors and nonlinear Kerr parameters of the resonances exploited by the probe and control signals.

	Probe ($m = 13$)	Control ($m = 14$)
λ_0 (nm)	1550.72	1486.57
Q_{rad}	47 180	1.55×10^5
Q_{intra}	1.94×10^5	2.17×10^5
$Q_{\mathrm{inter}}^{(0)}$	957	1 068
$Q_{\mathrm{e}}^{\mathrm{low}}$	4 846	9 005
$Q_{\mathrm{e}}^{\mathrm{upp}}$	10 520	21 850
Q_{tot}	729	906
$\Delta\omega_{\mathrm{intra}}$ (rad/s)	3.31×10^{10}	3.54×10^{10}
$\gamma_{\mathrm{SPM}}^{\mathrm{bulk}}$ (W^{-1}s^{-2})	4.70×10^{22}	5.33×10^{22}
$\gamma_{\mathrm{SPM}}^{\mathrm{gr}}$ (W^{-1}s^{-2})	-9.00×10^{23}	-8.19×10^{23}
$\gamma_{\mathrm{XPM}}^{\mathrm{bulk}}$ (W^{-1}s^{-2})	4.88×10^{22}	
$\gamma_{\mathrm{XPM}}^{\mathrm{gr}}$ (W^{-1}s^{-2})	-8.56×10^{23}	

B. Impact of Carrier Diffusion and Finite Relaxation Time on Routing Performance

Next, the nonlinear response of the resonator is studied by feeding the parameters of Table I in the framework of Sec. II B. First, the effect of SA finite relaxation time τ_{c} is examined separately from carrier diffusion. Diffusion is artificially switched-off by setting $D = 0$ in Eq. (2). We consider two cases of the finite relaxation time: $\tau_{\mathrm{c}} = 0.5$ ps and $\tau_{\mathrm{c}} = 1.67$ ps, both of which are typical values for graphene in the literature. They correspond to saturation intensities of $I_{\mathrm{sat}} = 3.35$ MW/cm^2 and $I_{\mathrm{sat}} = 1$ MW/cm^2, respectively, according to Eq. (3). The carrier saturation density is set to the typical value $N_{\mathrm{sat}} = 1.5 \times 10^{15}$ m^{-2}.[34]

The CW probe transmission curves for the through and drop output ports for both choices of relaxation time τ_{c} are depicted in Fig. 2(a). We are mainly concerned with the control input power required for reaching the critical coupling condition where the through-port transmission is zeroed out. It is found to be $P_{\mathrm{in},(c)} = 7.59$ mW when $\tau_{\mathrm{c}} = 0.5$ ps and $P_{\mathrm{in},(c)} = 2.88$ mW when $\tau_{\mathrm{c}} = 1.67$ ps. As anticipated, a shorter SA relaxation time results in higher saturation intensity and subsequently higher input power requirements: a roughly threefold increase in $P_{\mathrm{in},(c)}$ for a threefold decrease in τ_{c}. Note that the $P_{\mathrm{in},(c)}$ ratio between the two cases is not exactly equal to the I_{sat} ratio due to the nonuniformity of the electric field intensity (Fig. 1). We should also note that the operating wave-

Journal of Applied Physics
ACCEPTED MANUSCRIPT
AIP Publishing
This is the author's peer reviewed, accepted manuscript. However, the online version of record will be different from this version once it has been copyedited and typeset.
PLEASE CITE THIS ARTICLE AS DOI: 10.1063/5.0076959

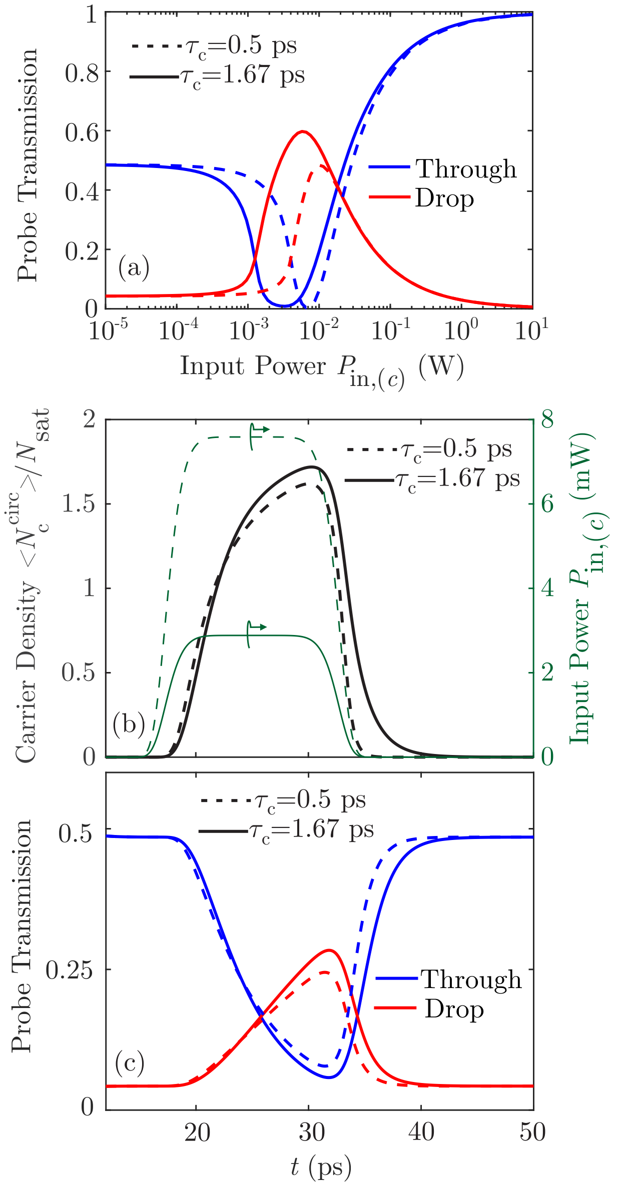

Figure 2. Steady state response. (a) CW transmission of the probe wave for both output ports as a function of control input power for two different values of SA finite relaxation time: $\tau_c = 0.5$ ps and $\tau_c = 1.65$ ps. (b, c) Dynamic response for a pulsed control wave. (b) Control input power and spatially-averaged photo-generated carrier density on the outer boundary of the disk resonator (normalized to N_{sat}). (c) Probe transmission in both through and drop ports vs time. Carrier diffusion is artificially switched-off ($D = 0$).

lengths have to be slightly blue-shifted in order to compensate for the frequency shifts induced by the Kerr effect and $\Delta\omega_{\mathrm{intra}}$ (Table I) at the critical coupling point. More specifically, we have used $\lambda_{(p)} = 1550.59$ nm and $\lambda_{(c)} = 1486.49$ nm when $\tau_c = 0.5$ ps, while $\lambda_{(p)} = 1550.66$ nm and $\lambda_{(c)} = 1486.52$ nm when $\tau_c = 1.67$ ps. It is also important to note the insertion loss (IL) and extinction ratio (ER) of the routing element in both through and drop ports. More specifically, in the through port we have $\mathrm{IL}_{(\mathrm{th})} \sim 3$ dB and $\mathrm{ER}_{(\mathrm{th})} > 20$ dB, while in the drop port $\mathrm{IL}_{(\mathrm{dr})} \sim 3$ dB and $\mathrm{ER}_{(\mathrm{dr})} \sim 10$ dB for both cases of the SA finite relaxation time considered ($\tau_c = 0.5$ ps, $\tau_c = 1.67$ ps).

The effect of finite relaxation time on the dynamic response can be assessed by considering a simple routing scenario, as illustrated in Fig. 2(b,c). A fourth-order super-Gaussian control input pulse with duration of 15 ps (FWHM) is used. The peak power is chosen so that the critical coupling condition is met for each case of τ_c. In Fig. 2(b) the spatially-averaged carrier density along the circumference of the resonator, $\langle N_c^{\mathrm{circ}} \rangle = \langle N_c(\rho = R) \rangle$, is depicted normalized to N_{sat}. Due to the presence of the coupling regions, the E-field norm and carrier distributions are not azimuthally symmetric justifying the exercised spatial averaging. In Fig. 2(c) we depict the respective probe transmission curves. It becomes evident that the delay in the leading edges of the transmitted pulses and the photo-generated carriers is dictated by the cavity photon lifetime ($Q_{\mathrm{tot}}^{m=14} = 906$, $\tau = 2Q/\omega_0 = 1.43$ ps), as the curves corresponding to different values of τ_c practically coincide with each other. This is well justified as our graphene SA model presumes that carriers are generated instantaneously. On the other hand, when the input pulse is switched off the delay in the trailing edges of the respective pulses is mainly determined by τ_c, as lower values of τ_c result in faster carrier relaxation and, thus, faster temporal response. It is also worth mentioning that the zero through-port transmission point [predicted in Fig. 2(a)] is not reached in Fig. 2(c) as a result of the short duration control input pulses injected in the resonant configuration. For more details about the effect of SA finite relaxation time on the all-optical routing element's bandwidth see Supplement, Sec. S3.

Having examined the effect of τ_c, we now turn to the study of carrier diffusion. Graphene has been experimentally observed to exhibit a rather high diffusion coefficient $D = 5500$ cm^2/s.[33] As for graphene relaxation time, we henceforth adopt the value $\tau_c = 1.67$ ps, which corresponds to the most typical value of graphene saturation intensity $I_{\mathrm{sat}} = 1$ MW/cm^2. In Fig. 3(a) the CW (steady-state) photo-generated carrier distribution on graphene is depicted for the control input power that satisfies the critical coupling condition. Carriers that are generated near the circumference of the resonator, where the mode is confined [Fig. 1(a)] are spread across the entire graphene plane due to diffusion. Compared to the absence of diffusion, this leads to a decrease of the carrier density at the position of the resonant mode. This fact is reflected in the CW transmission curves [Fig. 3(b)], where we compare the system in the presence of diffusion or when it is artificially switched off. When diffusion is taken into account, higher input power is required to obtain the same level of carrier density near the resonator circumference and effectively quench graphene losses. Specifically, we find that a roughly twofold increase in input power is required, as $P_{\mathrm{in},(c)} = 5.75$ mW

ACCEPTED MANUSCRIPT

Journal of Applied Physics

AIP Publishing

This is the author's peer reviewed, accepted manuscript. However, the online version of record will be different from this version once it has been copyedited and typeset.

PLEASE CITE THIS ARTICLE AS DOI: 10.1063/5.0076959

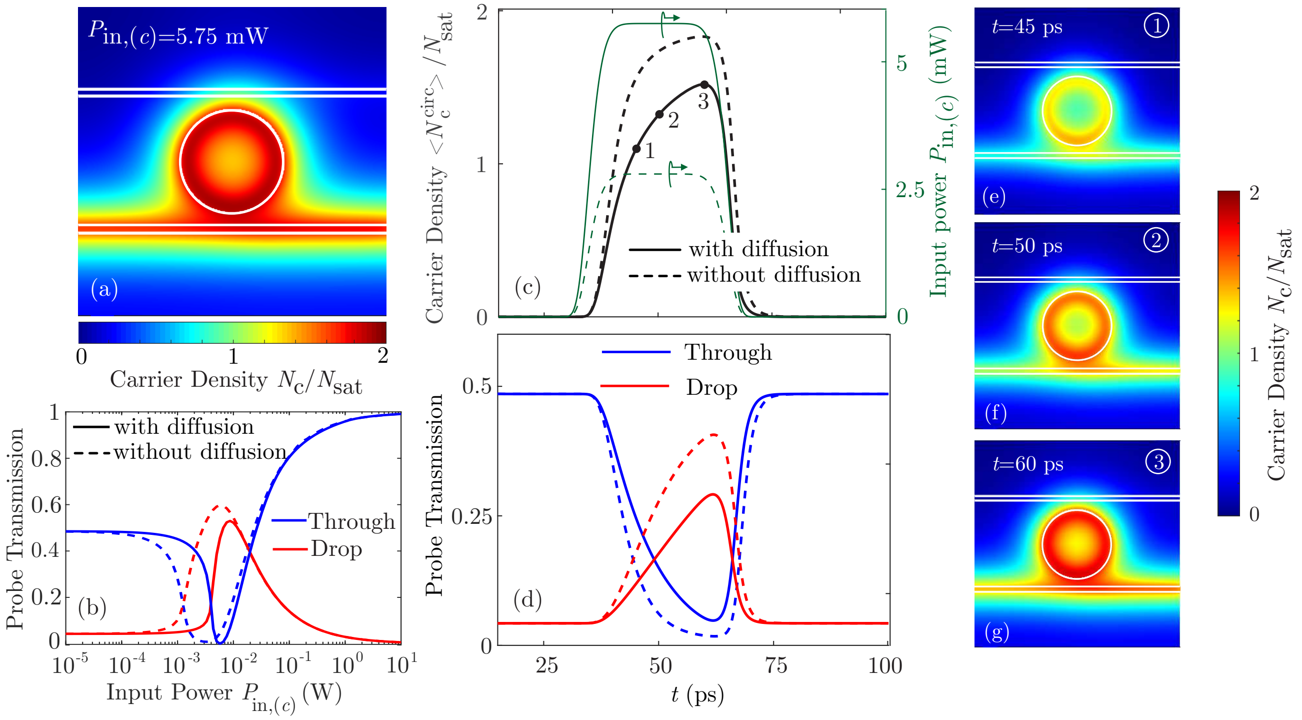

Figure 3. (a,b) Steady-state response with and without carrier diffusion. (a) CW carrier distribution on graphene for the control input power required to meet the critical coupling condition. (b) CW probe transmission curves vs control input power for both output ports. (c-g) Dynamic response under a pulsed control wave with and without carrier diffusion. (c) Control input power and corresponding mean value of the photo-generated carriers in the circumference of the resonator. (d) Probe transmission in through and drop ports as a function of time. Evolution of carrier distribution on graphene in the presence of diffusion: (e) $t = 45$ ps, (f) $t = 50$ ps, and (g) $t = 60$ ps. We have assumed $\tau_c = 1.65$ ps (and $I_{\mathrm{sat}} = 1$ MW/cm^2) throughout.

when $D = 5500$ cm^2/s and $P_{\mathrm{in},(c)} = 2.88$ mW when $D = 0$. In addition, diffusion results in steeper changes in the transmission curves. Finally, we note that the operating wavelengths are now $\lambda_{(p)} = 1550.61$ nm and $\lambda_{(c)} = 1486.50$ nm when $D = 5500$ cm^2/s, while $\lambda_{(p)} = 1550.66$ nm and $\lambda_{(c)} = 1486.52$ nm when $D = 0$. The IL and ER metrics for the through and drop ports remain practically the same as those obtained in Fig. 2(a) both in the presence and in the absence of carrier diffusion.

Carrier diffusion leads to substantial changes in the CW response. This is a direct consequence of the highly confined electric field in the circumference of the resonator (Fig. 1). Carrier diffusion can be suppressed if graphene is patterned into a narrow annular strip covering the circumference of the resonator, where the mode is confined. In this case, carriers cannot diffuse though the boundary [zero outward current (Neumann) boundary condition]. For details see Supplement, Sec. S4.

Finally, we examine the effect of carrier diffusion on the dynamic routing operation [Fig. 3(c,d)]. A fourth-order super-Gaussian control input pulse with duration of 30 ps (FWHM) is used. The temporal evolution of carrier density on the outer boundary of the resonator (spatially averaged and normalized) is depicted in Fig. 3(c) and the corresponding transmission curves for both output ports in Fig. 3(d). We find that carrier diffusion results in more pronounced delay (leading edge) and distortion of the transmitted pulses; in this case, the spatio-temporal effects of diffusion along with the loaded cavity photon lifetime shape the complex temporal dynamics. In Fig. 3(e-g) the carrier distribution is depicted for three different time instances marked in Fig. 3(c), to track the temporal evolution. As the control input pulse is applied, light is gradually coupled to the resonator and carriers are generated with the maximum of the density located in the coupling region between the feeding (lower) waveguide and the resonator [$t = 45$ ps, Fig. 3(e)]. For $t = 50$ ps [Fig. 3(f)], carriers diffuse further away from the resonator and the waveguide. At $t = 60$ ps when the normalized carrier density of Fig. 3(c) reaches its peak, the carrier distribution of Fig. 3(g) has reached values approaching $2N_{\mathrm{sat}}$ along the entire circumference and resembles the CW distribution of Fig. 3(a). For more details about the impact of carrier diffusion on the component's bandwidth see Supplement, Sec. S3.

C. Impact of Graphene Kerr Effect

In this Section, we try to separate and clarify the effect of nonlinear refraction and its impact on the overall nonlinear response of the resonator. To this end, in Fig. 4 we

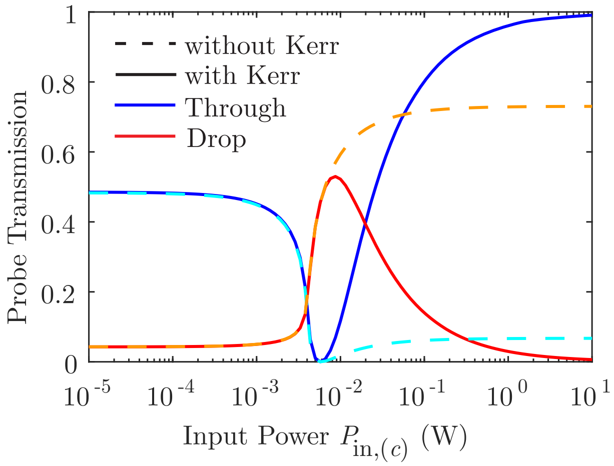

Figure 4. CW probe transmission curves in through and drop ports as a function of control input power. Carrier diffusion is considered. Dashed lines correspond to the case when nonlinear refraction (Kerr effect) is neglected. The Kerr effect starts to impact the response for powers above 6 mW (transmission minumum).

plot with dashed curves the CW probe transmission as a function of $P_{\mathrm{in},(c)}$ after artificially switching off the Kerr effect in graphene and bulk materials [$\Delta\omega_{\mathrm{Kerr},(k)} = 0$ in Eq. (6a)]. For easier comparison, we include with solid curves results when the Kerr effect considered; the same curves have been originally presented in Fig. 3(b). It is evident that SA is the dominant nonlinear effect for input powers up to those required for reaching the critical coupling point (transmission minimum), as solid and dashed lines coincide with each other. For higher input powers, solid and dashed lines begin to deviate, implying that the Kerr effect has a significant contribution to the overall nonlinear response. Furthermore, note that the presence of the Kerr effect requires an appropriate pre-shifting of the operating wavelengths in order to compensate the Kerr-induced nonlinear shift of the resonant wavelengths as in Sec. III B. This is important if the zero through-port transmission point is to be reached when the critical coupling condition is met. We also note that an appropriate pre-shifting should also be applied in order to cancel the linear shift in resonant wavelength induced by the imaginary part of σ_{intra} (Table I).

It is very interesting to examine the possibility of canceling out the Kerr effect contribution by counterbalancing the nonlinear shifts induced by graphene and the core material. This will result in a more clear response of the proposed component. Examining the nonlinear Kerr parameters compiled in Table I, it is apparent that the parameter γ for graphene is one order of magnitude greater (absolute value) than that of bulk materials (predominantly silicon). Consequently, the Kerr effect in graphene solely determines nonlinear refraction in the resonator. Note also that the signs are, as expected, opposite. Nevertheless, silicon can be replaced with a different self-focusing ($n_2 > 0$) material with higher nonlinear but similar linear refractive index, capable of cancelling out the negative γ^{gr}. Such a material is silicon-rich nitride, which possesses a nonlinear refractive index of $n_2^{\mathrm{SRN}} = 2.8 \times 10^{-17}$ m^2/W, one order of magnitude higher than silicon in the 1550 nm wavelength region.[38,39] SRN has attracted significant interest in recent years for nonlinear optics[38–42] since it has the additional advantage of a higher energy bandgap than silicon, prohibiting two-photon transitions at 1550 nm and, thus, TPA and FCEs. Although, such effects were omitted as negligible in the silicon-based structure studied thus far (the operating power was sufficiently low), they fundamentally limit the nonlinear response of silicon-based devices for higher powers. Furthermore, the linear refractive index of SRN is $n_0^{\mathrm{SRN}} = 3.1$[38,39] and therefore the SRN/SiO$_2$ index contrast is high enough for small footprint devices to be realized.

We thus replace silicon with SRN and redesign the initial structure [Fig. 1(a)], concluding to a resonator with radius $R = 2.46$ μm. The probe and control modes are now of azimuthal order $m = 19$ and $m = 20$, respectively, and have similar Q_{rad} values as the respective modes of the SOI-based resonator (cf. Table II and I). The height of the resonator is equal to 340 nm and the waveguide width is 200 nm, as previously. Calculating the nonlinear Kerr parameters of the SRN/SiO$_2$-based resonator we obtain for the probe mode $\gamma_{\mathrm{SPM}}^{\mathrm{bulk}} = +2.51 \times 10^{23}$ W^{-1}s^{-2} and $\gamma_{\mathrm{SPM}}^{\mathrm{gr}} = -7.39 \times 10^{23}$ W^{-1}s^{-2} (the other parameters follow the same trend as well). It is evident that the nonlinear Kerr parameter corresponding to the bulk materials (dominantly SRN) has been increased by almost one order of magnitude compared to the respective parameter of the SOI-based resonator, cf. Table I. Nevertheless, graphene still dominates the Kerr response as $|\gamma_{\mathrm{SPM}}^{\mathrm{gr}}| \sim 3 \times \gamma_{\mathrm{SPM}}^{\mathrm{bulk}}$. In order to make these parameters equal (in absolute value), we can slightly distance graphene from the resonator surface; the space between them is occupied by silica (inset of Fig. 5). By doing so, the interaction between E-field and graphene is weakened, thus leading to a decrease of $|\gamma_{\mathrm{SPM}}^{\mathrm{gr}}|$. We have found that the required height to make $|\gamma_{\mathrm{SPM}}^{\mathrm{gr}}| \sim \gamma_{\mathrm{SPM}}^{\mathrm{bulk}}$ is 50 nm. The resonator radius is also adjusted to 2.428 μm for the probe mode ($m = 19$) to have a resonant wavelength equal to $\lambda_{0,(p)} \sim 1550$ nm. Furthermore, the coupling gaps between the lower and upper waveguides and the resonator are determined to be 416 nm and 510 nm, respectively. The resonant wavelengths, quality factors and nonlinear Kerr parameters for the resonances exploited by the probe ($m = 19$) and control ($m = 20$) waves, as evaluated by linear simulations with COMSOL Multiphysics®, are summarized in Table II.

It is evident that the total nonlinear SPM Kerr parameters have been reduced by one order of magnitude (10^{22} W^{-1}s^{-2} instead of 10^{23}) and the XPM one by two orders of magnitude, in comparison with the SOI-based resonator, thus substantially suppressing the Kerr effect. This is seen Fig. 5, where the CW probe transmission curves are depicted with and without including the Kerr

ACCEPTED MANUSCRIPT

Journal of Applied Physics

AIP Publishing

This is the author's peer reviewed, accepted manuscript. However, the online version of record will be different from this version once it has been copyedited and typeset.

PLEASE CITE THIS ARTICLE AS DOI: 10.1063/5.0076959

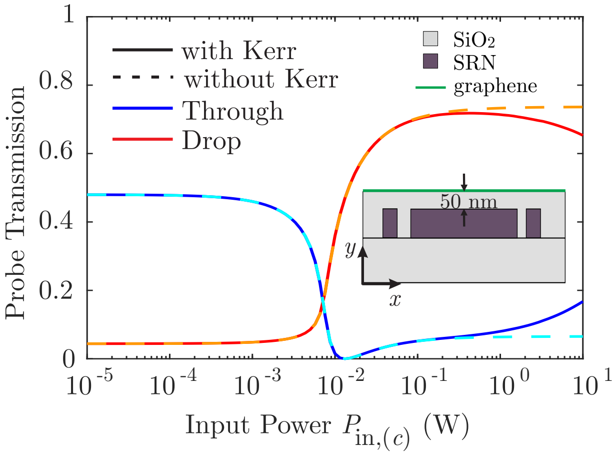

Figure 5. CW probe transmission curves vs control input power for through and drop ports of the SRN/SiO$_2$-based system. Solid (dashed) lines correspond to the case when nonlinear refraction (Kerr effect) is considered (neglected). Carrier diffusion is taken into account. Inset: Cross-section of SRN/SiO$_2$-based resonator at the xy plane bisecting the disk (cf. Fig. 1). Graphene is distanced from the resonator top surface and the space in between is occupied by silica. The required gap in order for $|\gamma_{\mathrm{SPM}}^{\mathrm{gr}}| \sim \gamma_{\mathrm{SPM}}^{\mathrm{bulk}}$ is approximately 50 nm.

Table II. Resonant wavelengths, quality factors and nonlinear Kerr parameters of the resonances exploited by probe and control waves for the SRN/SiO$_2$-based resonator.

	Probe ($m = 19$)	Control ($m = 20$)
λ_0 (nm)	1550.43	1505.74
Q_{rad}	57 690	1.43×10^5
Q_{intra}	2.37×10^5	2.61×10^5
$Q_{\mathrm{inter}}^{(0)}$	1 170	1 287
$Q_{\mathrm{e}}^{\mathrm{low}}$	5 825	8 394
$Q_{\mathrm{e}}^{\mathrm{upp}}$	12 470	19 690
Q_{tot}	886	1 044
$\Delta\omega_{\mathrm{intra}}$ (rad/s)	2.90×10^{10}	2.72×10^{10}
$\gamma_{\mathrm{SPM}}^{\mathrm{bulk}}$ ($\mathrm{W^{-1}s^{-2}}$)	2.51×10^{23}	2.82×10^{23}
$\gamma_{\mathrm{SPM}}^{\mathrm{gr}}$ ($\mathrm{W^{-1}s^{-2}}$)	-2.77×10^{23}	-2.53×10^{23}
$\gamma_{\mathrm{SPM}}^{\mathrm{total}}$ ($\mathrm{W^{-1}s^{-2}}$)	-2.60×10^{22}	2.90×10^{22}
$\gamma_{\mathrm{XPM}}^{\mathrm{bulk}}$ ($\mathrm{W^{-1}s^{-2}}$)	2.64×10^{23}	
$\gamma_{\mathrm{XPM}}^{\mathrm{gr}}$ ($\mathrm{W^{-1}s^{-2}}$)	-2.66×10^{23}	
$\gamma_{\mathrm{XPM}}^{\mathrm{total}}$ ($\mathrm{W^{-1}s^{-2}}$)	-2.00×10^{21}	

effect. The Kerr effect begins to have a non-negligible impact on the CW curves for input power exceeding 1 W, as opposed to few mW in Fig. 4. We also note that in the SRN/SiO$_2$-based resonator, the zero through-port transmission point can be reached without pre-shifting the operating wavelengths, since Kerr-induced frequency shifts are no longer significant. However, the input power requirement to satisfy the critical coupling condition suffers a roughly two-fold increase, as a result of the weakened graphene-light interaction. More specifically, the required control input power in the SRN/SiO$_2$-based resonator is $P_{\mathrm{in},(c)} = 13.2$ mW, instead of $P_{\mathrm{in},(c)} = 5.75$ mW in the silicon-based counterpart. The IL and ER metrics that are evaluated in this configuration are once again practically the same as those obtained in Fig. 2(a).

Suppressing the Kerr effect can be also accomplished by appropriately increasing the height of the resonator, without the need to distance graphene from the upper resonator surface. By increasing the resonator height, the mode is better confined in the cavity and light-graphene interaction is weakened, thus making it possible to satisfy the relation $\gamma_{\mathrm{gr}} + \gamma_{\mathrm{bulk}} \sim 0$. The reduced light-graphene interaction leads once again to increased power requirements for the control wave. For details see Supplement, Sec. S5.

IV. CONCLUSION

To recapitulate, we have expanded the capabilities of the conventional perturbation theory/temporal coupled-mode theory nonlinear framework to include the dynamics of graphene saturable absorption, exploiting a phenomenological model attributing SA to the saturation of the photo-generated carrier density in the conduction band of graphene. The carrier density is described with a spatio-temporal carrier rate equation incorporating the effects of SA finite relaxation time and carrier diffusion.

The expanded framework developed in this work has been applied in a practical graphene-enhanced SOI disk resonator, capable of operating as an all-optical routing and switching element in a two-wave excitation scheme. The effects of SA finite relaxation time and carrier diffusion on the overall nonlinear response of the resonator have been thoroughly investigated, both separately and collectively, in CW and pulsed operations. We have found that the relaxation time directly affects the saturation intensity and, consequently, the required input power for SA to manifest. In addition, the relaxation time was found to affect mainly the trailing edges of the transmitted pulses due to carrier relaxation; carrier photo-generation is instantaneous and thus the leading edges were affected mainly by the photon lifetime. Carrier diffusion has been found to result in greater input power requirements and increased delay and distortion of the transmitted pulses. Finally, we have studied the impact of the Kerr effect on the overall response of the resonator and it is found to be non-negligible as the power increases. A practical avenue to suppress the Kerr effect has been suggested by replacing silicon with silicon-rich nitride, which has similar linear optical properties but a higher nonlinear refractive index. Interplays with other linear and/or nonlinear effects, such as the thermo-optic effect (TOE) induced by the absorbed power due to the ohmic losses of the underlying materials, might also appear. Nevertheless, TOE response time is dictated by thermal diffusion, acquiring a time constant in the μs range. Thus, it cannot follow the ps-scale changes induced by the applied pulses, it is considered as constant

ACCEPTED MANUSCRIPT
Journal of Applied Physics
AIP Publishing
This is the author's peer reviewed, accepted manuscript. However, the online version of record will be different from this version once it has been copyedited and typeset.
PLEASE CITE THIS ARTICLE AS DOI: 10.1063/5.0076959

over time and, hence, it can be effectively counterbalanced.

We conclude that all of the studied effects have to be taken carefully into account for accurately assessing the power requirements and temporal dynamics of the all-optical routing operation. Our results contribute to the understanding of carrier dynamics and their impact on the CW and pulsed operation. The developed framework can be exploited to gain physical insight, efficiently study practical graphene-based switching components, and design high performance prototypes, before resorting to heavy full-wave nonlinear simulations and costly fabrication.

SUPPLEMENTARY MATERIAL

See Supplementary Material for supporting content. More specifically, the incorporation of the SA model in the temporal CMT equations is presented in more detail, in addition to the nonlinear Kerr parameters of both graphene and bulk materials. A different design approach in which the critical coupling condition is met at the low power (linear) regime is also discussed. Moreover, further simulation results are provided regarding the pulsed operation of the proposed routing element including an estimate of its bandwidth. In addition, we examine the dependence of carrier diffusion on graphene's spatial extend when it is patterned. Finally, an alternative approach to suppress the Kerr effect in the SRN/SiO_2-based resonator is investigated.

ACKNOWLEDGMENTS

The research work was supported by the Hellenic Foundation for Research and Innovation (H.F.R.I.) under the "First Call for H.F.R.I. Research Projects to support Faculty members and Researchers and the procurement of high-cost research equipment grant." (Project Number: HFRI-FM17-2086)

DATA AVAILABILITY STATEMENT

The data that support the findings of this study are available from the corresponding author upon reasonable request.

CONFLICT OF INTEREST

The authors have no conflicts to disclose.

REFERENCES

[1] K. S. Novoselov, V. I. Fal'Ko, L. Colombo, P. R. Gellert, M. G. Schwab, and K. Kim, "A roadmap for graphene," Nature **490**, 192–200 (2012).

[2] A. H. Castro Neto, F. Guinea, N. M. Peres, K. S. Novoselov, and A. K. Geim, "The electronic properties of graphene," Reviews of Modern Physics **81**, 109–162 (2009), arXiv:0709.1163.

[3] M. Liu, X. Yin, E. Ulin-Avila, B. Geng, T. Zentgraf, L. Ju, F. Wang, and X. Zhang, "A graphene-based broadband optical modulator," Nature **474**, 64–67 (2011).

[4] G. Sinatkas, T. Christopoulos, O. Tsilipakos, and E. E. Kriezis, "Comparative Study of Silicon Photonic Modulators based on Transparent Conducting Oxide and Graphene," Physical Review Applied **12**, 1 (2019).

[5] J. You, Y. Luo, J. Yang, J. Zhang, K. Yin, K. Wei, X. Zheng, and T. Jiang, "Hybrid/integrated silicon photonics based on 2D materials in optical communication nanosystems," Laser & Photonics Reviews **14**, 2000239 (2020).

[6] G. Sinatkas, T. Christopoulos, O. Tsilipakos, and E. E. Kriezis, "Electro-optic modulation in integrated photonics," Journal of Applied Physics **130**, 010901 (2021).

[7] J. L. Cheng, N. Vermeulen, and J. E. Sipe, "Third-order nonlinearity of graphene: Effects of phenomenological relaxation and finite temperature," Phys. Rev. B **91** (2015), 10.1103/PhysRevB.91.235320, arXiv:1503.07564.

[8] S. A. Mikhailov, "Quantum theory of the third-order nonlinear electrodynamic effects of graphene," Physical Review B **93**, 1–29 (2016), arXiv:1506.00534.

[9] N. Vermeulen, D. Castelló-Lurbe, J. Cheng, I. Pasternak, A. Krajewska, T. Ciuk, W. Strupinski, H. Thienpont, and J. Van Erps, "Negative Kerr Nonlinearity of Graphene as seen via Chirped-Pulse-Pumped Self-Phase Modulation," Physical Review Applied **6**, 1–7 (2016), arXiv:1611.07750.

[10] E. Dremetsika, B. Dlubak, S.-P. Gorza, C. Ciret, M.-B. Martin, S. Hofmann, P. Seneor, D. Dolfi, S. Massar, P. Emplit, and P. Kockaert, "Measuring the nonlinear refractive index of graphene using the optical kerr effect method," Optics Letters **41**, 3281 (2016).

[11] G. Xing, H. Guo, X. Zhang, T. C. Sum, and C. H. A. Huan, "The Physics of ultrafast saturable absorption in graphene," Optics Express **18**, 4564 (2010).

[12] A. Marini, J. D. Cox, and F. J. García De Abajo, "Theory of graphene saturable absorption," Physical Review B **95**, 1–11 (2017), arXiv:1605.06499.

[13] Q. Bao, H. Zhang, Y. Wang, Z. Ni, Y. Yan, Z. X. Shen, K. P. Loh, and D. Y. Tang, "Atomic-layer craphene as a saturable absorber for ultrafast pulsed lasers," Advanced Functional Materials **19**, 3077–3083 (2009).

[14] Z. Sun, T. Hasan, F. Torrisi, D. Popa, G. Privitera, F. Wang, F. Bonaccorso, D. M. Basko, and A. C. Ferrari, "Graphene mode-locked ultrafast laser," ACS Nano **4**, 803–810 (2010), arXiv:0909.0457.

[15] Q. Bao, H. Zhang, Z. Ni, Y. Wang, L. Polavarapu, Z. Shen, Q. H. Xu, D. Tang, and K. P. Loh, "Monolayer graphene as a saturable absorber in a mode-locked laser," Nano Research **4**, 297–307 (2011).

[16] M. Takahashi, W. Ueda, N. Goto, and S. Yanagiya, "Saturable absorption by vertically inserted or overlaid monolayer graphene in optical waveguide for all-optical switching circuit," IEEE Photonics Journal **5**, 6602109 (2013).

[17] M. Ono, M. Hata, M. Tsunekawa, K. Nozaki, H. Sumikura, H. Chiba, and M. Notomi, "Ultrafast and energy-efficient all-optical switching with graphene-loaded deep-subwavelength plasmonic waveguides," Nature Photonics **14**, 37–43 (2020).

[18] T. Christopoulos, V. G. Ataloglou, and E. E. Kriezis, "All-optical nanophotonic resonant element for switching and routing applications exploiting graphene saturable absorption,"

Journal of Applied Physics
ACCEPTED MANUSCRIPT
AIP Publishing
This is the author's peer reviewed, accepted manuscript. However, the online version of record will be different from this version once it has been copyedited and typeset.
PLEASE CITE THIS ARTICLE AS DOI: 10.1063/5.0076959

Journal of Applied Physics **127** (2020), 10.1063/5.0004552.

[19] H. Wang, N. Yang, L. Chang, C. Zhou, S. Li, M. Deng, Z. Li, Q. Liu, C. Zhang, Z. Li, and Y. Wang, "CMOS-compatible all-optical modulator based on the saturable absorption of graphene," Photonics Research **8**, 468 (2020).

[20] K. Alexander, N. A. Savostianova, S. A. Mikhailov, D. Van Thourhout, and B. Kuyken, "Gate-Tunable Nonlinear Refraction and Absorption in Graphene-Covered Silicon Nitride Waveguides," ACS Photonics **5**, 4944–4950 (2018).

[21] P. Demongodin, H. El Dirani, J. Lhuillier, R. Crochemore, M. Kemiche, T. Wood, S. Callard, P. Rojo-Romeo, C. Sciancalepore, C. Grillet, and C. Monat, "Ultrafast saturable absorption dynamics in hybrid graphene/Si3N4 waveguides," APL Photonics **4** (2019), 10.1063/1.5094523.

[22] A. Malouf, O. Henderson-Sapir, S. Set, S. Yamashita, and D. J. Ottaway, "Two-photon absorption and saturable absorption of mid-IR in graphene," Applied Physics Letters **114**, 6–11 (2019), arXiv:1810.12981.

[23] S. A. Mikhailov, "Theory of the strongly nonlinear electrodynamic response of graphene: A hot electron model," Physical Review B **100**, 115416 (2019), arXiv:1908.04631.

[24] N. Vermeulen, D. Castelló-Lurbe, M. Khoder, I. Pasternak, A. Krajewska, T. Ciuk, W. Strupinski, J. L. Cheng, H. Thienpont, and J. Van Erps, "Graphene's nonlinear-optical physics revealed through exponentially growing self-phase modulation," Nature Communications **9** (2018), 10.1038/s41467-018-05081-z.

[25] D. Castelló-Lurbe, H. Thienpont, and N. Vermeulen, "Predicting Graphene's Nonlinear-Optical Refractive Response for Propagating Pulses," Laser & Photonics Reviews **14**, 1900402 (2020), arXiv:1910.01866.

[26] T. Christopoulos, O. Tsilipakos, G. Sinatkas, and E. E. Kriezis, "Degenerate four-wave mixing in nonlinear resonators comprising two-dimensional materials: A coupled-mode theory approach," Physical Review B **98**, 1–10 (2018).

[27] L. A. Falkovsky, "Optical properties of graphene and IV–VI semiconductors," Physics-Uspekhi **51**, 887–897 (2008).

[28] G.W. Hanson, "Dyadic Green's functions for an anisotropic nonlocal model of biased graphene," IEEE Transactions on Antennas and Propagation **56**, 747–757 (2008).

[29] D. Chatzidimitriou and E. E. Kriezis, "Light propagation in nanophotonic waveguides considering graphene's saturable absorption," Physical Review A **102** (2020), 10.1103/PhysRevA.102.053512.

[30] E. Malic, T. Winzer, E. Bobkin, and A. Knorr, "Microscopic theory of absorption and ultrafast many-particle kinetics in graphene," Phys. Rev. B **84** (2011), 10.1103/PhysRevB.84.205406.

[31] J. M. Dawlaty, S. Shivaraman, M. Chandrashekhar, F. Rana, and M. G. Spencer, "Measurement of ultrafast carrier dynamics in epitaxial graphene," Applied Physics Letters **92** (2008), 10.1063/1.2837539, arXiv:0712.0119.

[32] M. Breusing, S. Kuehn, T. Winzer, E. Malić, F. Milde, N. Severin, J. P. Rabe, C. Ropers, A. Knorr, and T. Elsaesser, "Ultrafast nonequilibrium carrier dynamics in a single graphene layer," Phys. Rev. B **83**, 1–4 (2011).

[33] B. A. Ruzicka, S. Wang, J. Liu, K.-P. Loh, J. Z. Wu, and H. Zhao, "Spatially resolved pump-probe study of single-layer graphene produced by chemical vapor deposition [Invited]," Optical Materials Express **2**, 708 (2012), arXiv:1204.5732.

[34] F. Zhang, S. Han, Y. Liu, Z. Wang, and X. Xu, "Dependence of the saturable absorption of graphene upon excitation photon energy," Applied Physics Letters **106**, 1–6 (2015).

[35] T. Christopoulos, O. Tsilipakos, and E. E. Kriezis, "Low-power bistability in graphene-comprising 3D photonic resonant circuits," Journal of Applied Physics **122**, 1–12 (2017).

[36] T. Christopoulos, O. Tsilipakos, N. Grivas, and E. E. Kriezis, "Coupled-mode-theory framework for nonlinear resonators comprising graphene," Physical Review E **94**, 062219 (2016).

[37] O. Tsilipakos, T. Christopoulos, and E. E. Kriezis, "Long-range hybrid plasmonic disk resonators for mW bistability and self-pulsation," J. Lightw. Technol. **34**, 1333–1343 (2016).

[38] T. Wang, D. K. Ng, S. K. Ng, Y. T. Toh, A. K. Chee, G. F. Chen, Q. Wang, and D. T. Tan, "Supercontinuum generation in bandgap engineered, back-end CMOS compatible silicon rich nitride waveguides," Laser and Photonics Reviews **9**, 498–506 (2015).

[39] J. W. Choi, B. U. Sohn, G. F. Chen, D. K. Ng, and D. T. Tan, "Soliton-effect optical pulse compression in CMOS-compatible ultra-silicon-rich nitride waveguides," APL Photonics **4** (2019), 10.1063/1.5113758.

[40] C. Lacava, S. Stankovic, A. Khokhar, T. Bucio, F. Gardes, G. Reed, D. Richardson, and P. Petropoulos, "Si-rich Silicon Nitride for Nonlinear Signal Processing Applications," Scientific Reports **7**, 1–13 (2017).

[41] M. R. Dizaji, C. J. Krückel, A. Fülöp, P. A. Andrekson, V. Torres-Company, and L. R. Chen, "Silicon-rich nitride waveguides for ultra-broadband nonlinear signal processing," Opt. Express **25**, 12100–12108 (2017).

[42] X. Wang, X. Guan, S. Gao, H. Hu, L. K. Oxenløwe, and L. H. Frandsen, "Silicon/silicon-rich nitride hybrid-core waveguide for nonlinear optics," Optics Express **27**, 23775 (2019).

DOI: 10.1063/5.0076959

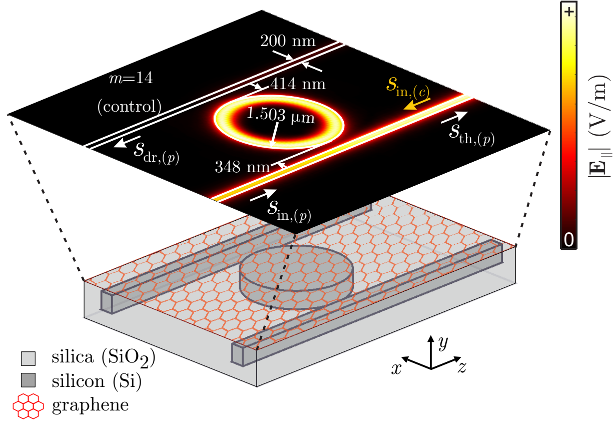
200 nm
414 nm
m=14
(control)
1.503 μm
348 nm
$S_{\mathrm{in},(c)}$
$S_{\mathrm{th},(p)}$
$S_{\mathrm{dr},(p)}$
$S_{\mathrm{in},(p)}$
$|\mathbf{E}_{\|}|$ (V/m)
+
0
silica (SiO$_2$)
silicon (Si)
graphene
x
y
z

Journal of Applied Physics
ACCEPTED MANUSCRIPT
AIP Publishing
This is the author's peer reviewed, accepted manuscript. However, the online version of record will be different from this version once it has been copyedited and typeset.
PLEASE CITE THIS ARTICLE AS DOI: 10.1063/5.0076959

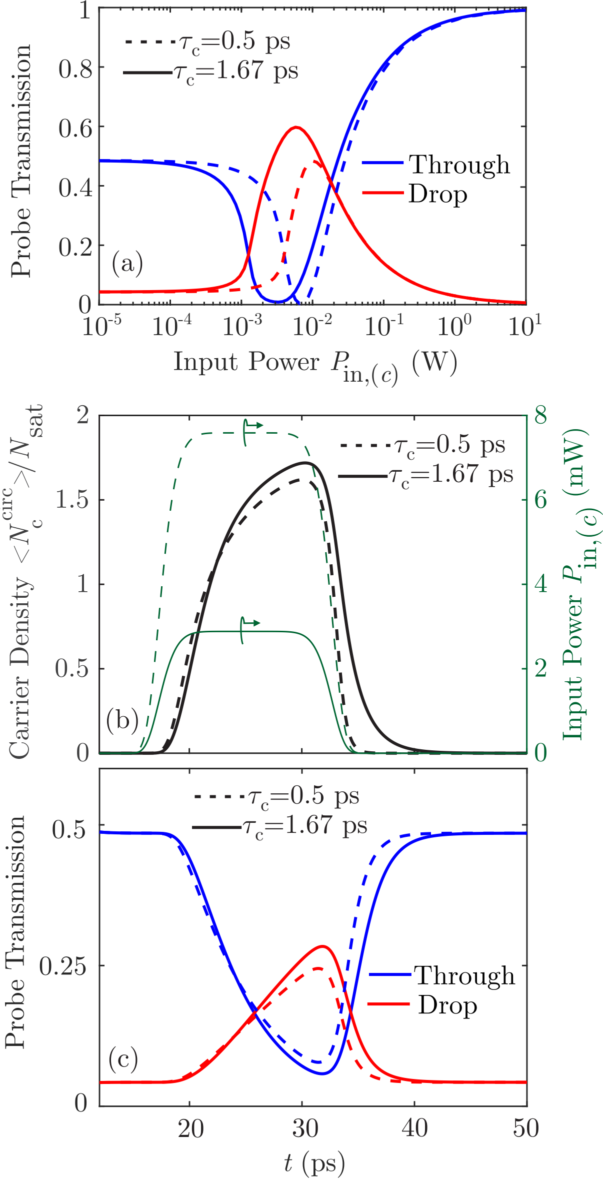

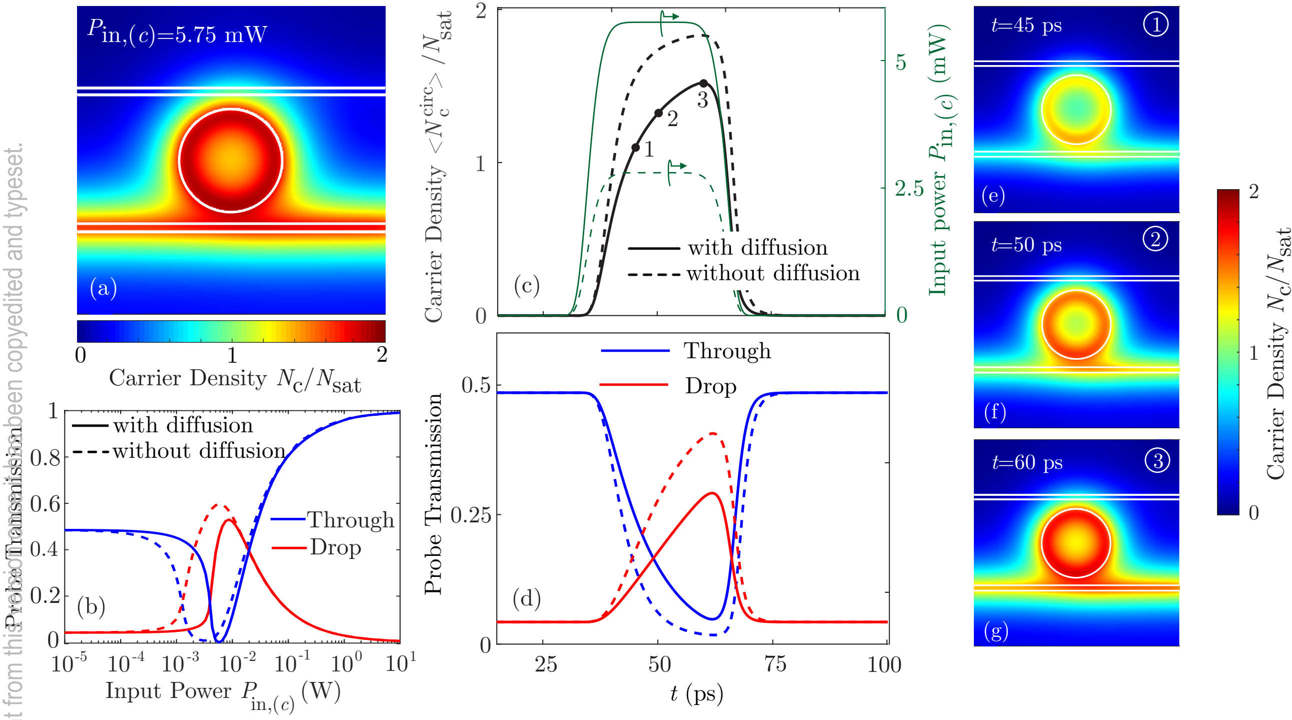
$P_{\mathrm{in},(c)}$=5.75 mW
(a)
0
1
2
Carrier Density N_c/N_{sat}
(b)
with diffusion
without diffusion
Through
Drop
Probe Transmission
0
0.2
0.4
0.6
0.8
1
10^{-5} 10^{-4} 10^{-3} 10^{-2} 10^{-1} 10^{0} 10^{1}
Input Power $P_{\mathrm{in},(c)}$ (W)
(c)
Carrier Density $<N_c^{circ}>/N_{sat}$
0
1
2
1
2
3
with diffusion
without diffusion
Input power $P_{\mathrm{in},(c)}$ (mW)
0
2.5
5
(d)
Through
Drop
Probe Transmission
0
0.25
0.5
25
50
75
100
t (ps)
t=45 ps ①
(e)
t=50 ps ②
(f)
t=60 ps ③
(g)
Carrier Density N_c/N_{sat}
0
1
2

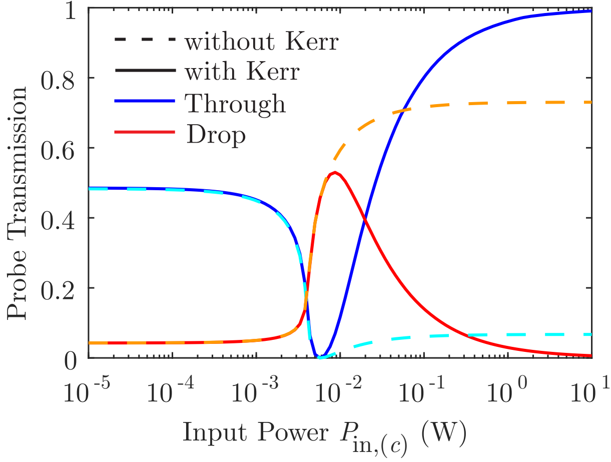
without Kerr
with Kerr
Through
Drop
Probe Transmission
0
0.2
0.4
0.6
0.8
1
10^{-5}
10^{-4}
10^{-3}
10^{-2}
10^{-1}
10^{0}
10^{1}
Input Power $P_{\mathrm{in},(c)}$ (W)

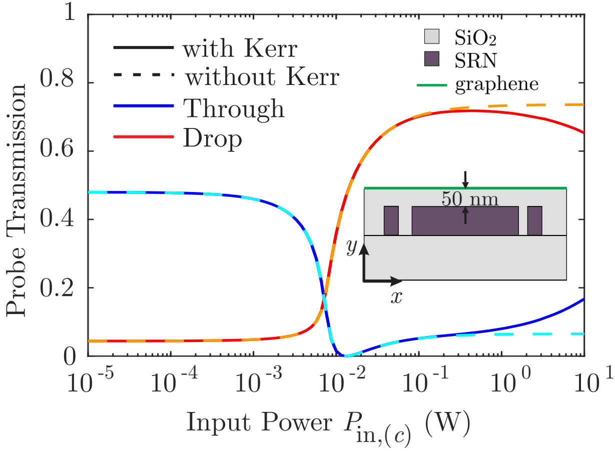Journal of Applied Physics
ACCEPTED MANUSCRIPT
AIP Publishing
This is the author's peer reviewed, accepted manuscript. However, the online version of record will be different from this version once it has been copyedited and typeset.
PLEASE CITE THIS ARTICLE AS DOI: 10.1063/5.0076959